Modelling Simul. Mater. Sci. Eng. **8** (2000) 515–540. Printed in the UK PII: S0965-0393(00)14483-3

Modelling and experimental analysis of vacuum plasma spraying. Part II: prediction of temperatures and velocities of plasma gases and Ti particles in a plasma jet

Y Y Zhao†, P S Grant and B Cantor
Oxford Centre for Advanced Materials and Composites, Department of Materials, University of Oxford, Parks Road, Oxford OX1 3PH, UK

E-mail: y.y.zhao@liv.ac.uk

Received 2 January 2000, accepted for publication 31 May 2000

Abstract. A numerical model has been developed to calculate the spatial distributions of plasma gas temperature, enthalpy, velocity and fractions of dissociated and ionized species in a vacuum plasma spraying (VPS) plasma jet under a range of plasma current, Ar flow rate, H_2 flow rate and chamber pressure, and the trajectories, temperatures and velocities of Ti particles under typical processing conditions. The model uses FLUENT V4.2 commercial software, incorporating approximations to describe dissociation, ionization and recombination reactions in the plasma jet. The calculations show that the spatial distributions of plasma gas temperature, enthalpy, velocity, and degrees of dissociation and ionization in the plasma jet are mainly controlled by the initial boundary values at the plasma gun exit, which are functions of the VPS processing conditions. The model predicts that the plasma jet length increases with increasing plasma current and decreasing Ar flow rate and chamber pressure, and shows a maximum with varying H_2 flow rate, agreeing well with measurements. Particle trajectory is largely determined by the initial particle position at the plasma gun exit. Particle temperature and velocity increase rapidly in the first 100 mm of the plasma jet and then become nearly constant at axial distances >150 mm. Particle temperature and velocity in the plasma jet decrease with increasing particle size and initial radial position at the plasma gun exit.

Nomenclature

A	particle surface area
a_1	constant
a_2	constant
a_3	constant
C_D	drag coefficient
C_p	specific heat of particle
C_i	specific heat of species i
D	particle diameter
dP_H	incremental increase of H partial pressure
dP_{H^+}	incremental increase of H^+ partial pressure
F_{Ar}	Ar flow rate
F_D	drag force per unit particle mass
F_{H_2}	H_2 flow rate

† Present address: Materials Science and Engineering, Department of Engineering, The University of Liverpool, Brownlow Hill, Liverpool L69 3GH, UK.

0965-0393/00/040515+26$30.00

G_a reaction rate of Ar^+ recombination
G_b reaction rate of H^+ recombination
G_c reaction rate of H recombination
h enthalpy
h_i^0 formation enthalpy of species i
I plasma current
K_{Ar} reaction rate coefficient for Ar^+ recombination
K_H reaction rate coefficient for H^+ recombination
K_{H_2} reaction rate coefficient for H recombination
K_T cooling rate of plasma gas
k constant
$\overline{L}$ average plasma jet length
M_i net production rate of species i per unit volume in chemical reactions
m_i mass fraction of species i
m_p particle mass
n number of species
P plasma gas pressure
P_H partial pressure of H
P_{H^+} partial pressure of H^+
Pr Prandtl number of plasma gas mixture
Q dissociation or ionization energy
Q_{Ar} ionization energy of Ar
Q_H ionization energy of H
Q_{H_2} dissociation energy of H_2
R gas constant
r radial coordinate
Re relative Reynolds number
T plasma gas temperature
$\overline{T}$ mean initial plasma temperature at plasma gun exit
t time
T^0 reference temperature
T_L plasma temperature at plasma jet tip
T_p particle temperature
$\boldsymbol{v}$ plasma gas velocity vector
v_r radial velocity
$\boldsymbol{v}_p$ particle velocity vector
v_x axial velocity
$\overline{v}_x$ average plasma gas velocity throughout plasma jet
x axial coordinate
χ degree of dissociation or ionization
χ_H degree of ionization of H
Φ heat dissipation function
η convective heat transfer coefficient
κ plasma gas thermal conductivity
μ plasma gas viscosity

ρ plasma gas density
ρ_p particle density
τ stress tensor
τ_{rx} radial component of viscous stress
τ_{xr} axial component of viscous stress
∇ vector differential operator

1. Introduction

Atmospheric and vacuum plasma spraying (APS and VPS) are widely used to produce coatings of high melting point and highly reactive materials, and may also be used to manufacture particulate or fibre-reinforced ceramic or metal matrix composite deposits [1–8]. In order to produce optimum quality coatings and deposits of a range of materials, there has been considerable investigation of the effect of VPS processing on coating porosity, grain size, adhesion, surface roughness, hardness and process efficiency. Because there are a large number of interdependent VPS processing parameters available to operate or control, statistical methods such as the Taguchi method have been used in experimental design to reduce experimentation needed to optimize plasma spraying conditions [9–17]. Optimization of plasma spraying is therefore usually achieved by empirical means and there is still insufficient scientific understanding of the physical mechanisms controlling plasma gas and entrained particle behaviour [18–20].

Nonetheless, it is accepted that the microstructure and mechanical properties of plasma sprayed protective coatings and deposits are determined by the sizes, temperatures and velocities of the droplets in the spray at deposition which are determined by: (1) the temperature profile of the plasma jet; (2) the dwell times of the particles in the plasma jet; and (3) the efficiency of heat transfer from the hot plasma gas to the particles.

Experimental measurements of gas and particle temperatures and velocities in a plasma jet are difficult because of the extremely high temperatures and velocities, although some experimental data has been obtained using specialized techniques [21–23]. Therefore, in the absence of convenient experimental techniques, numerical modelling has been promoted as a method with which to investigate the fundamental behaviour of the plasma gas and particles, and as an aid to optimize the plasma spraying processing conditions. Efforts have been made to develop models to calculate the temperature and velocity profiles of the plasma jet and the trajectories, temperatures and velocities of the particles [21–52]. In some investigations, the plasma processes such as dissociation, ionization and recombination in the plasma jet were treated as chemical reactions in chemical and thermal equilibrium [23, 47, 52]. In other investigations, however, the plasma was assumed to be a hot gas jet and the effects of dissociation, ionization and recombination, which contribute strongly to the plasma enthalpy and accordingly particle melting, were neglected.

This paper is part II of a two part series. In part I, an analytical model was developed to calculate the plasma gas temperature, enthalpy, velocity and degrees of Ar and H ionization at a plasma gun exit as functions of the VPS processing parameters of plasma current, Ar flow rate, H_2 flow rate and chamber pressure [53]. The objective in part II is to describe a computational fluid dynamics (CFD) model to calculate:

(1) the resulting spatial distributions of plasma temperature, enthalpy, velocity, and fractions of dissociated and ionized species as the plasma jet exits the plasma gun and flows into the spray chamber; and

(2) the associated trajectories, temperatures and velocities of Ti particles injected into the plasma jet at the plasma gun exit.

The predictions from part I of the initial plasma properties at the plasma gun exit are used as inlet boundary conditions. Calculations are performed for a range of plasma current, Ar flow rate, H_2 flow rate, chamber pressure, particle size, and initial particle position and temperature, using commercial CFD software, FLUENT V4.2†, with approximations to incorporate the effect of plasma gas reactions and associated enthalpy change. The resulting predictions of plasma jet length are then compared with experimental measurements under corresponding processing conditions.

2. Experiment

Measurements of plasma jet length were performed in a Plasma Technik (now Sulzer Metco) A2000 system. The VPS procedure and typical spray conditions were as described in part I [53]. The plasma jet length was defined as the distance from the plasma gun to the visible tip of the flame when viewed by eye through an ultraviolet protective window. The jet length was determined by moving the plasma gun horizontally towards a stationary steel marker fixed vertically in the VPS chamber. The plasma gun was programmed to move at 10 mm increments towards the marker until the jet tip was judged to be touching the marker. The plasma jet length was then taken as the axial distance between the plasma gun tip and the marker. The plasma current, Ar flow rate, H_2 flow rate and chamber pressure were varied independently to investigate their effects on the plasma jet length. Clearly, this definition of jet length is arbitrary and requires further assumptions in order for comparison with model predictions. Based on previous work [54], the jet tip is defined as the point where the jet temperature is 3000 K, below which the plasma emission through the protective window is assumed to be no longer visible.

3. Numerical model

3.1. Basic assumptions

FLUENT V4.2 is a general purpose programme for modelling fluid flow, heat transfer and chemical reactions with or without a second phase in the flow. A plasma jet has different properties from an inert gas flow because of the dissociation, ionization and recombination plasma reactions. In part I [53], calculations of the initial plasma temperature, enthalpy, velocity, and degrees of ionization and dissociation at a plasma gun exit under a series of VPS processing conditions were performed assuming:

(1) the plasma is in local thermodynamic equilibrium;
(2) the degrees of plasma gas dissociation and ionization follow the Saha equation;
(3) the Ar+H_2 plasma gas specific heat capacity is a mixture of those of Ar and H_2 as functions of temperature;
(4) the radiation energy losses are negligible;
(5) the plasma obeys the ideal gas law; and
(6) plasma temperature and velocity are constant across the plasma gun exit.

For the additional calculations in part II, further assumptions are now needed.

(1) The plasma gun, substrate and chamber are static and symmetric about the plasma gun axis as shown schematically in figure 1. Therefore, the VPS process is treated as a

† FLUENT is a registered trademark of FLUENT Inc., Centerra Resource Park, 10 Cavendish Court, Lebanon, NH 03766, USA.

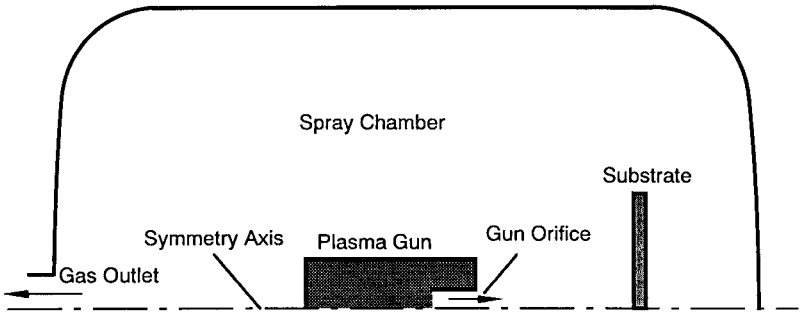

Figure 1. Schematic of the simplified geometry of the VPS system for numerical modelling.

Table 1. Thermal conductivity κ of Ar.

T(K)	313	333	353	373	393
$\kappa \times 10^2$ (W m^{-1} K^{-1})	1.677	1.729	1.781	1.850	1.902

Table 2. Viscosity μ of Ar.

T(K)	373	473	575	674	766	857	987	1060
$\mu \times 10^5$ (kg m^{-1} s^{-1})	2.695	3.223	3.685	4.115	4.484	4.815	5.257	5.632

two-dimensional problem. The distance between the plasma gun and the substrate is fixed at 300 mm. Because the plasma jet zone occupies a very much smaller volume than the chamber, the plasma gun robot and the turntable, which are integral parts of the experimental apparatus, are assumed to have little effect on the gas flow field between the plasma gun and the substrate.

(2) The plasma gas thermal conductivity and viscosity are taken to be:
   (i) independent of plasma gas composition;
   (ii) identical to those of the primary Ar; and
   (iii) predictable by linear extrapolation from low temperature, as shown in tables 1 and 2, respectively [55].

(3) Body forces, such as gravitational force, are negligible.

(4) Diffusion of species because of concentration gradients is negligible compared with the high gas velocities in the plasma jet.

(5) The dissociation and ionization of gases and the recombination of the dissociated atoms or ionized ions and electrons can be treated as standard thermodynamic chemical reactions.

(6) The injected Ti particles are spherical and are heated by convective heat transfer across the droplet boundary layer, with additional heating by radiation, electron bombardment and recombination of ions and electrons and dissociated atoms at the particle surface ignored.

(7) The Ti particles are assumed to obey Newtonian heat flow conditions, i.e. the rate of heating or cooling is determined by the surface heat transfer coefficient only, and internal heat conduction is sufficiently rapid that the particles are isothermal [21].

(8) The latent heats of solid state phase transformation (e.g. $\alpha \rightarrow \beta$) and melting or solidification of the Ti particles are not considered.

3.2. Governing equations

3.2.1. Plasma gases. The basic equations describing the plasma gas flow in cylindrical polar coordinates are as follows [56–58].

3.2.1.1. Conservation of mass. Assuming that there is no mass added to the continuous gas phase from the injection and motion of the second phase Ti particles, the rate of change of the fluid mass in any volume is equal to the overall fluid mass flux into the volume. The mass conservation equation is [56–58]

$$\frac{\partial \rho}{\partial t} = -\nabla \cdot (\rho \boldsymbol{v}) \tag{1}$$

where ρ is the local density of the plasma gas, t is the time, ∇ is the vector differential operator and $\boldsymbol{v}$ is the gas velocity vector. In equation (1), the left-hand side (LHS) is the rate at which mass is stored, and the right-hand side (RHS) is the net rate of mass influx.

In a fluid involving chemical reactions, the conservation of the constituent species must be considered. For a plasma gas composed of primary Ar and secondary H_2, and neglecting any free electrons, the species in the plasma jet are Ar, Ar^+, H_2, H and H^+. The conservation of species i is given by [58]

$$\frac{\partial}{\partial t}(\rho m_i) = -\nabla(\rho m_i \boldsymbol{v}) + M_i \tag{2}$$

where m_i is the mass fraction of species i and M_i is the net production rate of species i per unit volume by the different chemical reactions. In equation (2), the LHS is the rate at which the mass of species i is stored, and the first and second terms on the RHS are the net rate of influx of species i, and the rate at which species i is produced by reaction, respectively.

3.2.1.2. Conservation of momentum. The rate of change of momentum of fluid within any volume is equal to the total body and surface forces produced by external means and acting on the fluid volume. Neglecting external body forces, the momentum conservation equation is given by [56, 57]

$$\rho \frac{\mathrm{d}\boldsymbol{v}}{\mathrm{d}t} = -\nabla P + \nabla \cdot \boldsymbol{\tau} \tag{3}$$

where P is the pressure and $\boldsymbol{\tau}$ is the stress tensor, the components of which for an axisymmetric two-dimensional flow are [59]

$$\boldsymbol{\tau}_{wr} = \boldsymbol{\tau}_{rx} = \mu \left(\frac{\partial v_r}{\partial x} + \frac{\partial v_x}{\partial r} \right) \tag{4}$$

where μ is the plasma gas viscosity, and v_x and v_r are the axial x and radial r components of the velocity, respectively. In equation (3), the LHS is the rate at which momentum is stored, and the first and second terms on the RHS are the momentum influx because of surface forces from pressure and viscous forces exerted by the surrounding fluid, respectively.

3.2.1.3. Conservation of energy. The rate of change of fluid enthalpy within a volume is equal to the sum of the rate at which the heat is conducted into the fluid within the volume, the rate at which body and surface forces do work on the fluid and the rate at which heat is produced in the fluid. The energy conservation equation in terms of the enthalpy is given by [58]

$$\rho \frac{\mathrm{d}h}{\mathrm{d}t} = \nabla \cdot (\kappa \nabla T) + \frac{\mathrm{d}P}{\mathrm{d}t} + \Phi + \sum_{i=1}^{i=n} h_i^0 M_i \tag{5}$$

where h is the enthalpy, κ is the thermal conductivity of the plasma gas, T is the temperature, Φ is the heat dissipation function, n is the total number of different species and h_i^0 is the formation enthalpy of species i at a specified reference temperature T^0. The LHS is the rate of enthalpy change; the first term on the RHS is the rate at which heat is conducted into the fluid; the second and third terms on the RHS are the rates at which work is done on the fluid by the surface forces resulting from pressure and viscous forces exerted by the surrounding fluid, respectively; and the fourth term on the RHS is the rate at which enthalpy is released from chemical reactions. For an axisymmetric two-dimensional flow, the dissipation function is [59]

$$\Phi = 2\mu\left[\left(\frac{\partial v_x}{\partial x}\right)^2 + \left(\frac{v_r}{r}\right) + \left(\frac{\partial v_r}{\partial r}\right)^2 + \frac{1}{2}\left(\frac{\partial v_r}{\partial x} + \frac{\partial v_x}{\partial r}\right)^2\right]. \tag{6}$$

The enthalpy h is defined as

$$h = \sum_{i=1}^{i=n} m_i \int_{T^0}^{T} C_i \, \mathrm{d}T \tag{7}$$

where C_i is the specific heat of species i.

Because the plasma jet is usually turbulent [23, 50, 52], each velocity component in the above set of conservation equations is treated as a sum of a mean value and a fluctuating part which is calculated using the optional renormalized group theory (RNG) k–ϵ model in the FLUENT software [58]. The RNG k–ϵ model requires inputs of turbulent intensities and characteristic lengths at inlets and outlets. The turbulent intensity is usually between 2 and 12% [58] and is difficult to predict in the plasma jet because of large variations in plasma gas velocity. In this case, it is assumed to be 5%, regardless of specific processing conditions. The turbulent characteristic length at an inlet or outlet is assumed to be the equivalent radius of the inlet or outlet [58].

3.2.2. Ti particles. There is vigorous momentum and heat exchange between the injected Ti particles and the plasma gas. The basic equations describing a second phase particle in the gas flow are as follows [21, 58].

3.2.2.1. Momentum transfer. Neglecting additional body forces, the velocity of a particle can be calculated according to the force balance on the particle

$$\frac{\mathrm{d}\boldsymbol{v}_\mathrm{p}}{\mathrm{d}t} = F_\mathrm{D}(\boldsymbol{v} - \boldsymbol{v}_\mathrm{p}) \tag{8}$$

where $\boldsymbol{v}_\mathrm{p}$ and $\boldsymbol{v}$ are the particle and gas velocities, respectively, and F_D is the drag force per unit particle mass, which is given by

$$F_\mathrm{D} = \frac{18\mu}{\rho_\mathrm{p} D^2}\frac{C_\mathrm{D} Re}{24} \tag{9}$$

where ρ_p is the particle density, D is the particle diameter, C_D is the drag coefficient and Re is the relative Reynolds number defined as

$$Re = \frac{\rho D|\boldsymbol{v}_\mathrm{p} - \boldsymbol{v}|}{\mu}. \tag{10}$$

The drag coefficient C_D is a function of the relative Reynolds number

$$C_\mathrm{D} = a_1 + \frac{a_2}{Re} + \frac{a_3}{Re^2} \tag{11}$$

where a_1, a_2 and a_3 are constants given by Morsi and Alexander [58].

3.2.2.2. Heat transfer. Assuming that the particle is heated by convective heat transfer only, the temperature is uniform throughout the particle and there are no phase transformations in the particle, the particle temperature can be calculated from

$$m_{\mathrm{p}} C_{\mathrm{p}} \frac{\mathrm{d}T_{\mathrm{p}}}{\mathrm{d}t} = \eta A (T - T_{\mathrm{p}}) \tag{12}$$

where m_{p} is the mass of the particle, C_{p} is the specific heat of the particle, T_{p} is the particle temperature, A is the surface area of the particle, η is the convective heat transfer coefficient and T is the local gas temperature.

The heat transfer coefficient is evaluated using the Ranz–Marshall correlation [58]

$$\eta = \frac{\kappa (2.0 + 0.6 Re^{1/2} Pr^{1/3})}{D} \tag{13}$$

where $Pr = (\mu \sum m_i C_i)/\kappa$ is the Prandtl number of the plasma gas mixture.

3.3. Estimation of reaction rates

In a plasma gas composed of primary Ar and secondary H_2, the dissociation, ionization and recombination processes are:

$$\mathrm{Ar}^+ + \mathrm{e} \Leftrightarrow \mathrm{Ar} \qquad \mathrm{H}^+ + \mathrm{e} \Leftrightarrow \mathrm{H} \qquad \mathrm{H} + \mathrm{H} \Leftrightarrow \mathrm{H}_2. \tag{14}$$

Treating these processes as chemical reactions, the reaction rates of the Ar^+, H^+ and H recombinations, G_{a}, G_{b} and G_{c}, respectively, are required to calculate the net production rates of the species. Consider first the recombination of H^+ ions and electrons to form H atoms. The reaction rate G_{b} can be expressed by the variation of H partial pressure P_{H} with plasma temperature T along the plasma jet axis

$$G_{\mathrm{b}} = K_T \frac{\mathrm{d}P_{\mathrm{H}}}{\mathrm{d}T} \tag{15}$$

where K_T is the average cooling rate of the plasma gas flowing along the plasma jet, which is assumed to be a constant over the range of VPS processing conditions and is estimated as

$$K_T \approx \frac{(T_{\mathrm{L}} - \overline{T})\overline{v}_x}{\overline{L}} \approx -5 \times 10^7 \ \mathrm{K\ s^{-1}} \tag{16}$$

where $T_{\mathrm{L}} \approx 3000$ K is the assumed plasma temperature at the plasma jet tip [54], $\overline{T} \approx 11\,500$ K is an assumed average initial plasma temperature at the plasma gun exit [53], $\overline{v}_x \approx 1600$ m s^{-1} is an assumed average plasma gas velocity throughout the plasma jet [53] and $\overline{L} \approx 0.25$ m is an assumed typical plasma jet length based on experiments.

The H partial pressure is determined by the degree of ionization of H, and is related to H^+ partial pressure by [60]

$$P_{\mathrm{H}} = \frac{1 - \chi_{\mathrm{H}}}{\chi_{\mathrm{H}}} P_{\mathrm{H}^+} \tag{17}$$

where P_{H} is the H partial pressure, P_{H^+} is the H^+ partial pressure and χ_{H} is the degree of ionization of H, which is given by the Saha equation [60, 61]

$$\frac{\chi^2}{1 - \chi^2} = \frac{kT^{2.5}}{P} \mathrm{e}^{-Q/RT} \tag{18}$$

where χ is the degree of dissociation or ionization, k is a constant, $R = 8.31$ J K^{-1} mol^{-1} is the gas constant and Q is the dissociation or ionization energy. The ionization energies of Ar and H and the dissociation energy of H_2 are $Q_{\mathrm{Ar}} = 1.5206 \times 10^6$ J mol^{-1}, $Q_{\mathrm{H}} = 1.3117 \times 10^6$ J mol^{-1} and $Q_{\mathrm{H_2}} = 4.320 \times 10^5$ J mol^{-1}, respectively, [62].

As the incremental increase of H partial pressure equals to an incremental decrease of H^+ partial pressure, i.e. $dP_{H^+} = -dP_H$, the following equation can be derived from equation (17)

$$\frac{dP_H}{dT} = -\frac{P_{H^+}}{\chi_H}\frac{d\chi_H}{dT}. \tag{19}$$

The last RHS term of equation (19) can be derived from the Saha equation (18) as

$$\frac{d\chi_H}{dT} = \chi_H(1-\chi_H^2)\left(\frac{5}{4T} + \frac{Q_H}{2RT^2}\right). \tag{20}$$

Because the degree of ionization χ_H is usually considerably less than one and decreases with decreasing plasma temperature [53], $(1-\chi_H^2)$ is assumed to be unity. In addition, because the plasma temperature is usually lower than 14 000 K [53], $5/4T$ is much less than $Q_H/2RT^2$ and therefore is also assumed negligible. Combining equations (15), (16), (19) and (20), the reaction rate G_b is given by

$$G_b \approx -K_T\frac{Q_H}{2RT^2}P_{H^+} = \frac{K_H}{T^2}P_{H^+} \tag{21}$$

where $K_H = K_T Q_H/2R$ is the reaction rate coefficient for H^+ recombination, which is a constant determined by the H ionization energy and the temperature gradient in the plasma jet.

Similarly, the reaction rates of $Ar^+ + e \Leftrightarrow Ar$ and $H + H \Leftrightarrow H_2$, G_a and G_c are given by:

$$G_a \approx -K_T\frac{Q_{Ar}}{2RT^2}P_{Ar^+} = \frac{K_{Ar^+}}{T^2}P_{Ar^+} \tag{22}$$

$$G_c \approx -K_T\frac{Q_{H_2}}{4RT^2}P_H = \frac{K_{H_2}}{T^2}P_H. \tag{23}$$

Substituting the value of K_T from equation (16), the reaction rate coefficients for Ar^+, H^+ and H recombinations are $K_{Ar} = 4.57 \times 10^{12}$, $K_H = 3.94 \times 10^{12}$ and $K_{H_2} = 6.5 \times 10^{11}$ K^2 s^{-1}.

It should be noted that in deriving the reaction rate of the H recombination, G_c, the degree of H_2 dissociation is assumed to be considerably less than one. At low temperatures, this is true. At high temperatures, however, the degree of H_2 dissociation may approach one. As a result, equation (23) is an overestimate of the reaction rate of the H recombination. Because the reaction rate calculated by equation (23) at a high temperature is very small anyway, the simplification does not introduce significant errors into the calculations.

3.4. Calculation procedure

The solution of equations (1)–(23) was enabled using commercial CFD software FLUENT V4.2 on a SiliconGraphics Indy workstation. The calculation procedure included geometry set-up, control volume grid construction, assignment of boundary conditions, input of gas and particle properties, calculation and post data processing. Solution of the steady-state single-phase plasma gas flow in the spray chamber was obtained by discretization of equations (1)–(7) and (14)–(23) onto a curvilinear control volume grid followed by an implicit numerical procedure [58]. The solution of the dynamic and thermal behaviour of Ti particles in the gas flow was performed by application of equations (8)–(13). The momentum and heat exchange coupling between the disperse Ti particles and the continuous gas phase was accomplished by alternatively solving the steady-state single-phase gas flow equations, and then using a particle tracking technique to follow the trajectories of the Ti particles through the control volumes. The exchange of momentum and heat between the gas and the particles as they track through the control volumes were then incorporated in the re-calculation of the single phase flow as heat/momentum sinks or sources at each control volume. This procedure was repeated until the solutions for both phases had ceased to change significantly, and the solutions were assumed to be converged [58, 63].

Table 3. Variation of initial plasma gas temperature, velocity and degree of Ar and H ionization with VPS processing condition.

Plasma current (A)	Ar flow rate (l min^{-1})	H_2 flow rate (l min^{-1})	Chamber pressure (kPa)	Temperature (K)	Velocity (m s^{-1})	Degree of ionization Ar	Degree of ionization H
500	35	8	15	10 472	1780	0.025	0.083
700	35	8	15	11 913	2025	0.084	0.235
850	35	8	15	12 654	2151	0.141	0.359
950	35	8	15	13 081	2224	0.185	0.441
700	15	8	15	12 787	1321	0.154	0.384
700	25	8	15	12 299	1681	0.111	0.296
700	45	8	15	11 588	2356	0.066	0.191
700	35	0	15	11 743	1370	0.074	—
700	35	2	15	12 404	1613	0.119	0.314
700	35	4	15	12 283	1761	0.110	0.294
700	35	12	15	11 540	2270	0.063	0.185
700	35	8	5	11 299	5763	0.090	0.264
700	35	8	25	12 210	1245	0.081	0.222
700	35	8	35	12 410	904	0.079	0.212

3.5. Boundary conditions

As with all flows, meaningful modelling of the plasma jet depends critically on the correct assignment of the solution boundary conditions, which included: (1) temperature or heat flux, velocity or pressure and composition of the plasma gas at all boundaries; (2) turbulent quantities at inlet and outlet boundaries; and (3) initial particle sizes, mass flow rates, positions, temperatures and velocities at the inlet boundary and a description of the fate of particles on contact with other boundaries [58, 63].

The most critical boundary conditions are the plasma gas temperature, velocity and composition at the inlet, i.e. at the plasma gun exit orifice, which depend on the plasma gun nozzle geometry and on the VPS processing parameters. In this study, the aim was to investigate the effect of VPS processing conditions on plasma jet flow by systematically varying plasma current, Ar flow rate, H_2 flow rate and chamber pressure in the ranges 500–950 A, 15–45 l min^{-1}, 0–12 l min^{-1} and 5–35 kPa, respectively. Table 3 shows the initial plasma gas temperature, velocity and degree of Ar and H ionization at the plasma gun exit under this series of VPS processing conditions, calculated from the model previously described in part I [53]. At the plasma gun exit, H_2 is dissociated completely into H, which is then partly ionized. The turbulent intensity and characteristic length at the exit are assumed to be 5% and 6 mm, respectively.

The flow with Ti particles has been investigated for only one set of VPS conditions: plasma current $I = 700$ A, Ar flow rate $F_{Ar} = 35$ l min^{-1}, H_2 flow rate $F_{H_2} = 8$ l min^{-1} and chamber pressure $P = 15$ kPa. The Ti particles have a density of 4.5 g cm^{-3} and a constant specific heat of 528 J kg^{-1} K^{-1} [55], with a total assumed mass flow rate of 0.4 g s^{-1}, which is typical of VPS [2]. To simulate the pure Ti powders produced by Plasma Technik for VPS [64], the Ti particles are divided into five groups with sizes of 20, 60, 100, 150 and 250 μm and corresponding mass flow rates of 0.016, 0.084, 0.16, 0.08 and 0.06 g s^{-1}, and each group is further divided into 12 injections. In total, there are 60 particle injections at the plasma gun exit distributed evenly along the radius with a spacing of 0.1 mm as shown schematically in figure 2. Two different conditions of the injected particles are used to study their effects on the behaviour of the particles:

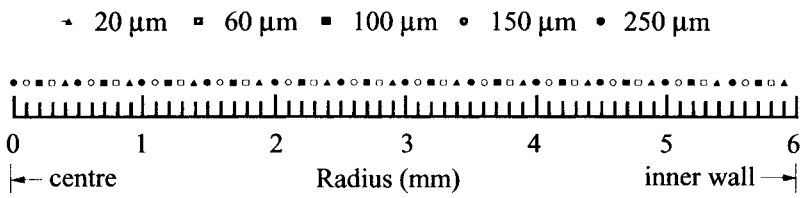

Figure 2. Sizes and initial positions of the Ti particle injections at the plasma gun exit.

(1) assuming that the particles have not been heated and accelerated before leaving the plasma gun exit, the initial temperature and velocity of the particles are room temperature and zero, respectively; and
(2) assuming that the particles have already been heated and accelerated to some extent by the hot plasma in the plasma gun before leaving the plasma gun exit, the initial temperature and velocity of the particles are 800 K and 10 m s^{-1}, respectively.

The plasma gun itself and the substrate are assumed to have no heat exchange with the plasma gas in the chamber. The chamber wall is water cooled and the temperature is constant at room temperature. The gas velocities at the plasma gun body, substrate and chamber wall surfaces are zero. At the outlet, the gas is assumed to be at room temperature and chamber pressure. The turbulent intensity and characteristic length at the outlet are assumed to be 5% and 40 mm, respectively. The secondary species Ar^+, H^+ and H are assumed to recombine completely at the outlet and the chamber wall to form Ar and H_2 with the same composition as the initial plasma gas. The Ti particles reaching the substrate, chamber wall and outlet are assumed to be trapped and thereafter exit the calculations.

4. Results and discussion

4.1. Spatial distribution of plasma properties without Ti particles

Figure 3 shows calculated plasma gas velocity vectors in the region between the plasma gun and the substrate without secondary particles for $I = 700$ A, $F_{Ar} = 35$ l min^{-1} (2.478×10^{-2} mol s^{-1}), $F_{H_2} = 8$ l min^{-1} (5.664×10^{-3} mol s^{-1}) and $P = 15$ kPa. The direction of the plasma gas velocity is primarily axial with only a small radial component, except near the substrate where the gas flow is diverted. The plasma gas velocity decreases rapidly along the axial direction, typically from ~2000 m s^{-1} at the plasma gun exit to ~400 m s^{-1} at an axial distance of 200 mm. The high-velocity plasma gas jet is confined to a narrow region between the plasma gun and substrate within a radius of ~30 mm.

Figures 4(a)–(e) show the calculated spatial distribution of the plasma gas temperature, enthalpy, and Ar^+, H and H^+ mole fractions in the region between the plasma gun and the substrate without second phase particles for the same conditions, i.e. for $I = 700$ A, $F_{Ar} = 35$ l min^{-1}, $F_{H_2} = 8$ l min^{-1} and $P = 15$ kPa. The Ar and H_2 mole fractions are not plotted, since the sum of the Ar and Ar^+ mole fractions is equal to the Ar mole fraction in the initial Ar + H_2 plasma gas mixture, and the sum of the H_2 mole fraction and half of the H and H^+ mole fractions is equal to the H_2 mole fraction in the initial Ar + H_2 mixture. The plasma gas temperature, enthalpy, and Ar^+, H and H^+ mole fractions all decrease with increasing axial distance from the plasma gun exit and increasing radial distance from the symmetric axis, with contours taking the shape of a long and narrow jet. The plasma gas temperature, enthalpy, and Ar^+, H and H^+ mole fractions are over 10 000 K, 1.3×10^7 J kg^{-1}, 0.05, 0.2 and

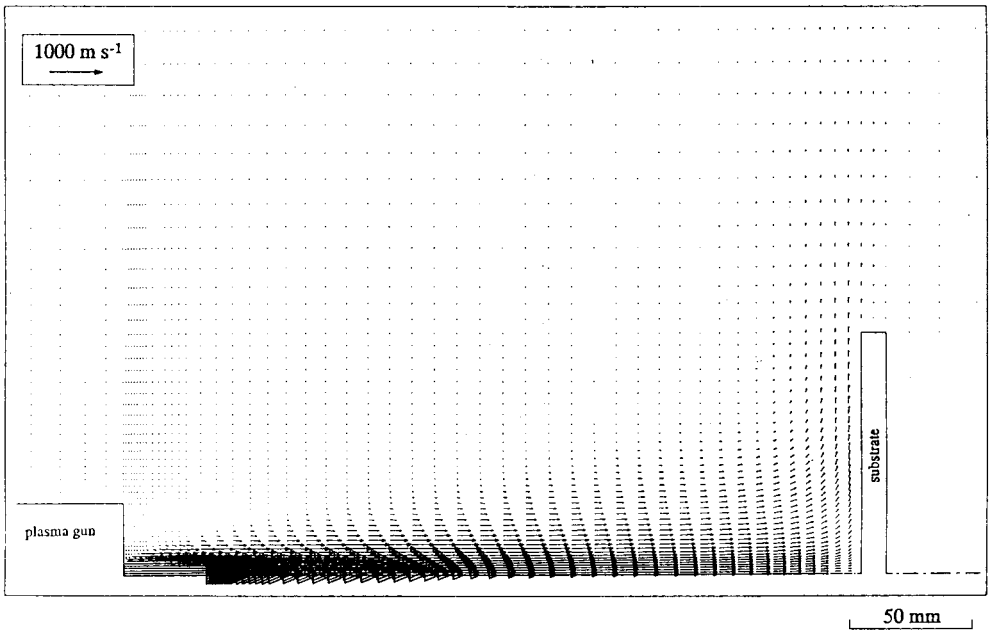

Figure 3. Spatial distribution of plasma gas velocity.

0.065, respectively, in the first 80 mm from the plasma gun exit at the axisymmetric centre, but decrease rapidly to 15–30% of their initial values when the axial distance increases to >150 mm or the radial distance increases to >20 mm.

4.2. Effects of processing conditions

4.2.1. Plasma current. Figures 5(a)–(f) show the plasma gas temperature, enthalpy, velocity, and Ar^+, H and H^+ mole fractions as functions of axial distance along the plasma jet axis, respectively, for different plasma currents of 500, 700, 850 and 950 A with constant $F_{Ar} = 35\,l\,min^{-1}$, $F_{H_2} = 8\,l\,min^{-1}$ and $P = 15$ kPa. The plasma gas temperature, enthalpy and velocity decrease with increasing distance, while Ar^+, H and H^+ mole fractions show plateaux up to 80 mm, and then decrease rapidly. The plasma gas temperature, enthalpy, velocity, and Ar^+ and H^+ mole fractions increase with increasing plasma current within the plateau region. The H mole fraction decreases with increasing plasma current in the same region. Beyond 80 mm, however, variations in plasma current do not have such a significant effect.

Figure 6 shows the variation of both calculated and measured plasma jet length with plasma current, using the assumptions described earlier. The calculations agree well with the experimental measurements. The plasma jet length increases nearly linearly with increasing plasma current, from ~120 mm at 300 A to ~260 mm at 1000 A.

Plasma gun operating conditions strongly affect the exit plasma gas temperature, enthalpy, velocity, and degrees of dissociation and ionization at the plasma gun exit [53], which determine the subsequent spatial distributions. Increasing plasma current increases the plasma energy input rate, and therefore increases the initial and downstream values of the plasma gas temperature, enthalpy, velocity, and Ar^+ and H^+ mole fractions in the plasma jet, as well as the plasma jet length. The H mole fraction decreases with increasing plasma current, because the sum of H and H^+ mole fractions is a constant due to complete H_2 dissociation

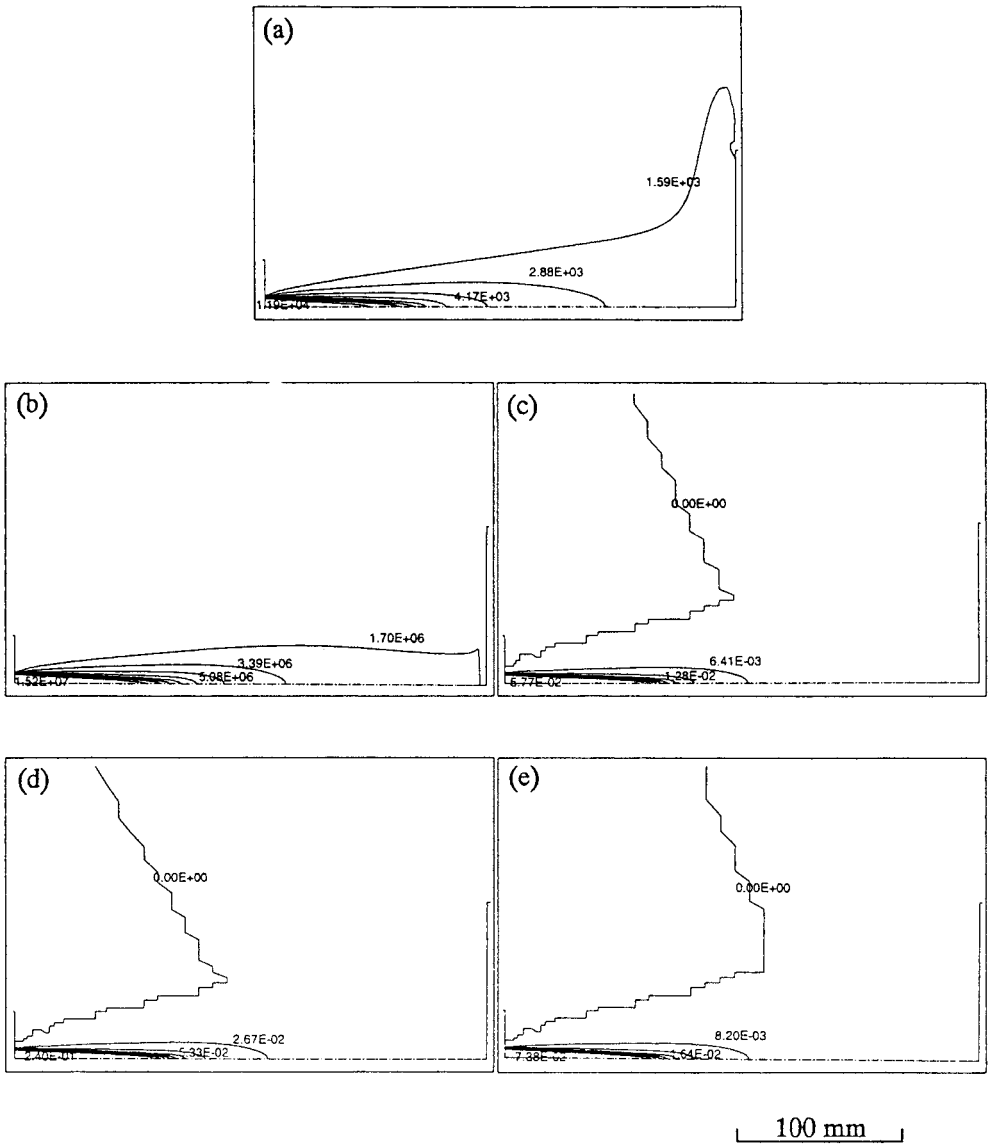

Figure 4. Spatial distribution of: (a) plasma gas temperature (K); (b) plasma gas enthalpy (J kg^{-1}); (c) Ar^+ mole fraction; (d) H mole fraction; and (e) H^+ mole fraction.

when temperatures are above 6000 K [53]. The variations of the Ar^+, H and H^+ mole fractions with axial distance from the plasma gun show plateaux in the first 80 mm in the plasma jet and sharp decreases thereafter. This is because the variations of the Ar^+, H and H^+ mole fractions are largely determined by the reaction rates of the Ar^+, H and H^+ recombinations, which are strongly temperature dependent. The form of the sharp transition at the end of the plateau regions might appear to arise from the computational procedure adopted in the calculations. However, this was demonstrated not to be true by examining the calculated values. The effect of plasma gas temperature on the mole fraction variations can be understood by considering the reaction rate G_b of the H^+ recombination. Combining equations (15) and (21), the variation

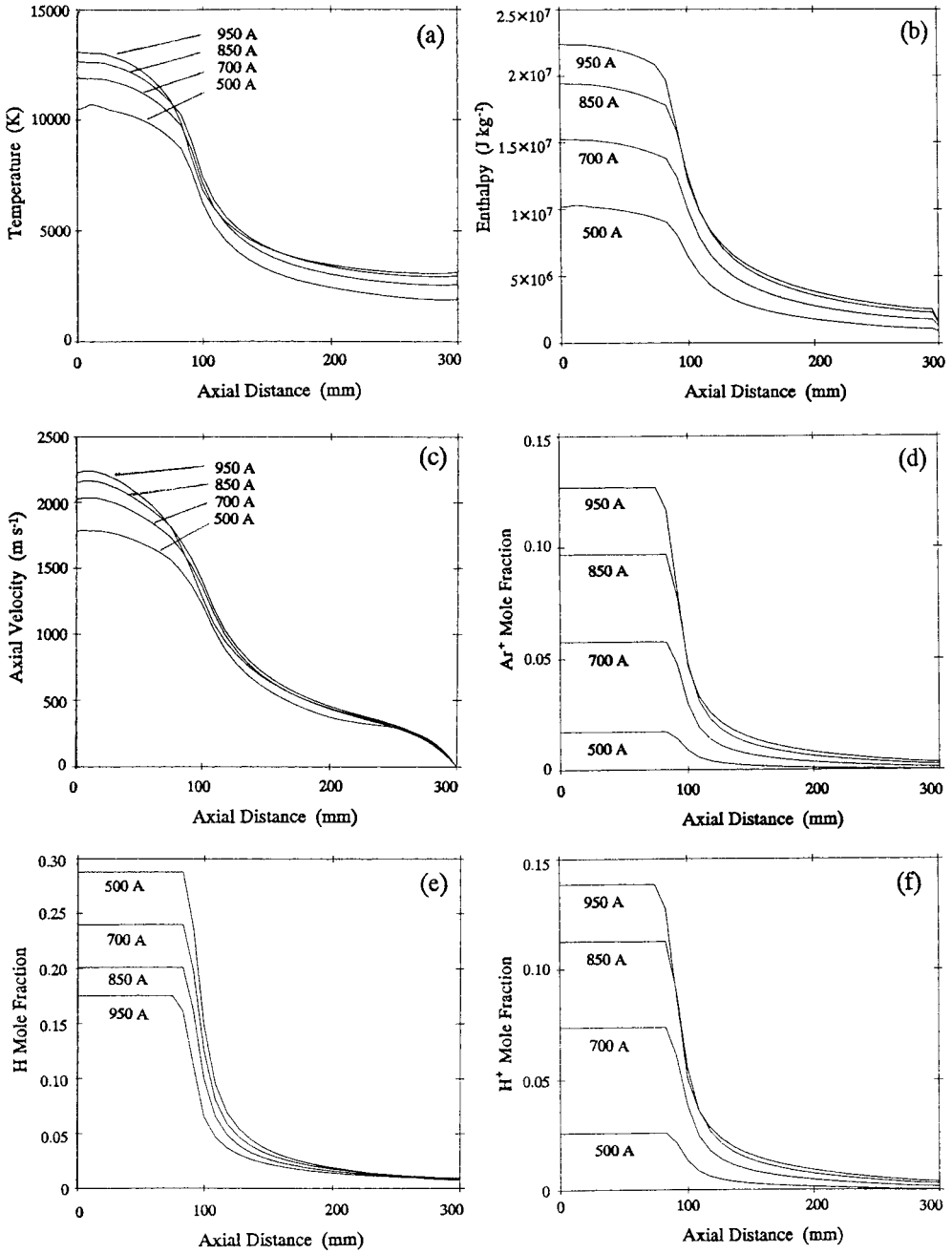

Figure 5. Distributions of: (a) temperature; (b) enthalpy; (c) axial velocity; (d) Ar^+ mole fraction; (e) H mole fraction; and (f) H^+ mole fraction along the plasma jet axis for different plasma currents.

of the H^+ partial pressure P_{H^+} with plasma temperature T along the plasma jet axis can be obtained as

$$\frac{dP_{H^+}}{dT} = -\frac{dP_H}{dT} = \frac{Q_H}{2RT^2} P_{H^+}.$$

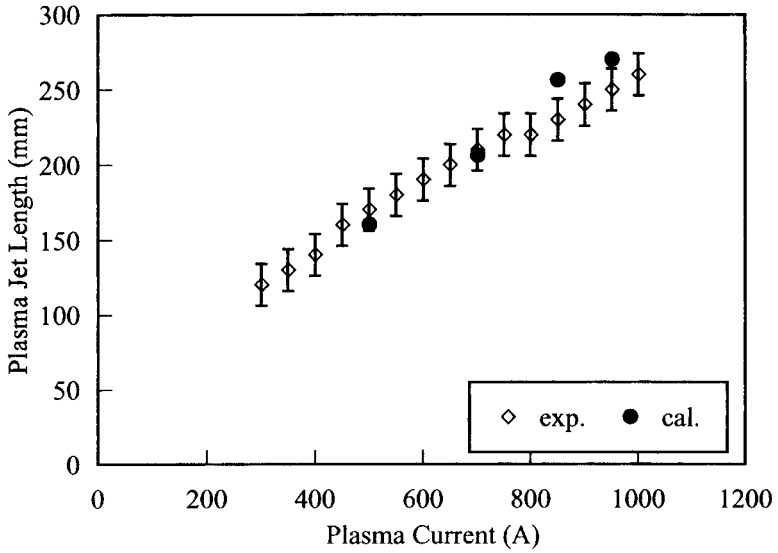

Figure 6. Relationship between plasma jet length and plasma current.

The relative variation of P_{H^+} along an infinitesimal axial distance corresponding to a temperature change dT is therefore

$$\frac{dP_{H^+}}{P_{H^+}} = \frac{Q_H dT}{2RT^2}.$$

Because the H^+ mole fraction is proportional to the H^+ partial pressure, the variation of the H^+ mole fraction within a small distance along the plasma jet axis is proportional to the variation of the plasma gas temperature and inversely proportional to the square of the mean plasma gas temperature. At axial distances <80 mm, the plasma gas temperatures are very high and the temperature changes are very small. As a consequence, there is little change in mole fractions of the species as a function of distance in the near nozzle region. When the axial distance increases to >80 mm, the plasma gas temperatures decrease rapidly. The resultant high recombination rates lead to a very sharp transition to the region of rapid decreases in mole fractions of the dissociated and ionized species. The temperature changes are extremely large when the axial distance increases from 80 to 100 mm. The grid in this region, however, is relatively coarse with a mean axial cell length of 10 mm, exaggerating the sudden change at the end of the plateau region.

4.2.2. Ar flow rate. Figures 7(a)–(f) show the variation of plasma gas temperature, enthalpy, velocity, and Ar^+, H and H^+ mole fractions as functions of axial distance along the plasma jet axis, respectively, for different Ar flow rates of 15, 25, 35 and 45 l min^{-1} with constant $I = 700$ A, $F_{H_2} = 8$ l min^{-1} and $P = 15$ kPa. With increasing Ar flow rate, the plasma gas temperature, enthalpy, and Ar^+, H and H^+ mole fractions all decrease at the plasma gun exit, but gradually turn to increase in the region between 50 and 150 mm from the plasma gun as shown in figures 7(a), (b) and (d)–(f). When the axial distance is longer than 200 mm, there is little effect of Ar flow rate. In contrast, the plasma gas velocity increases with increasing Ar flow rate at all axial distances as shown in figure 7(c).

Figure 8 shows the variation of both calculated and measured plasma jet length with increasing Ar flow rate. When the Ar flow rate is above 20 l min^{-1}, the plasma jet length does

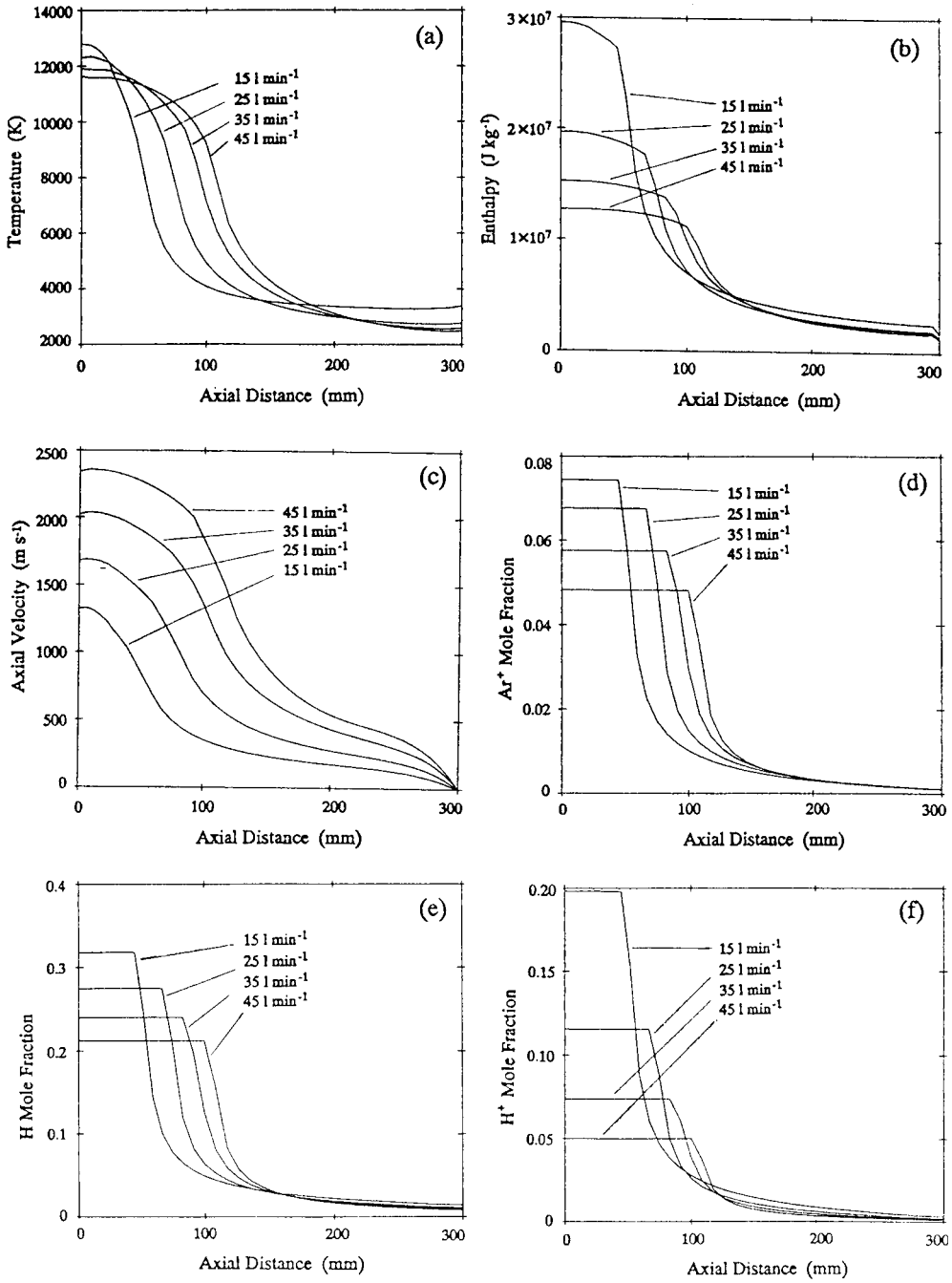

Figure 7. Distributions of: (a) temperature; (b) enthalpy; (c) axial velocity; (d) Ar^+ mole fraction; (e) H mole fraction; and (f) H^+ mole fraction along the plasma jet axis for different Ar flow rates.

not vary much with increasing Ar flow rate, and is in good agreement with the calculations. However, at a lower Ar flow rate of 15 l min^{-1}, the measured value of the plasma jet length is 240 mm whereas the calculated plasma jet length is 350 mm.

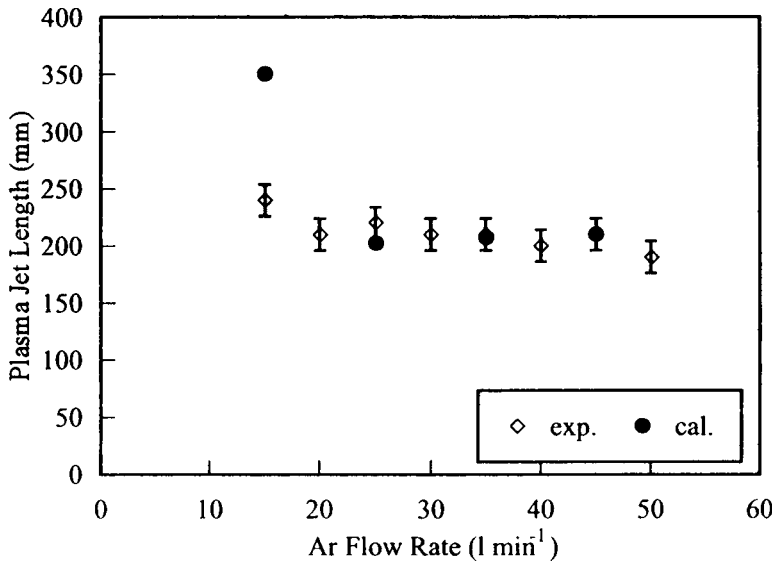

Figure 8. Relationship between plasma jet length and Ar flow rate.

As shown in part I, increasing Ar flow rate increases the plasma energy input rate and the initial plasma gas velocity, but decreases the initial plasma gas temperature, enthalpy and Ar^+, H and H^+ mole fractions [53]. With higher plasma gas velocities, recombination of dissociated and ionized species and the associated heat release occur at increased axial distances. Therefore, plasma gas temperature, enthalpy, and Ar^+, H and H^+ mole fractions at a given distance in the region between 50 and 150 mm increase slightly with increasing Ar flow rate.

4.2.3. H_2 flow rate. Figures 9(a)–(f) show the variation of plasma gas temperature, enthalpy, velocity, and Ar^+, H and H^+ mole fractions as functions of axial distance along the plasma jet axis, respectively, for different H_2 flow rates of 0, 2, 4, 8 and 12 l min^{-1} with constant $I = 700$ A, $F_{Ar} = 35$ l min^{-1} and $P = 15$ kPa. Figures 9(b), (c), (e) and (f) show that the plasma enthalpy, velocity, and H and H^+ mole fractions all increase with increasing H_2 flow rate. Figures 9(a) and (d) show that introducing 2 l min^{-1} H_2 increases the plasma temperature slightly and the Ar^+ mole fraction dramatically. However, for H_2 flow rates >2 l min^{-1} the plasma temperature and the Ar^+ mole fraction decrease progressively with increasing H_2 flow rate.

Figure 10 shows the variation of both calculated and measured plasma jet length with increasing H_2 flow rate. Both calculated and measured values increase on the addition of H_2 although calculated jet lengths show a more marked increase. On further H_2 additions, both calculated and measured values decrease, but once again the calculated jet lengths show a more marked response. The calculations over all H_2 flow rates agree reasonably well with the measurements.

Increasing H_2 flow rate increases the plasma energy input rate approximately parabolically, increases the plasma gas enthalpy, velocity and H and H^+ mole fractions, but increases and then decreases the initial plasma gas temperature and Ar^+ mole fraction, with peak values at a flow rate of $\sim$2 l min^{-1} [53]. Although the initial plasma temperature of a pure Ar plasma is comparable with that of an Ar+H_2 plasma, the temperature drops rapidly after an axial distance

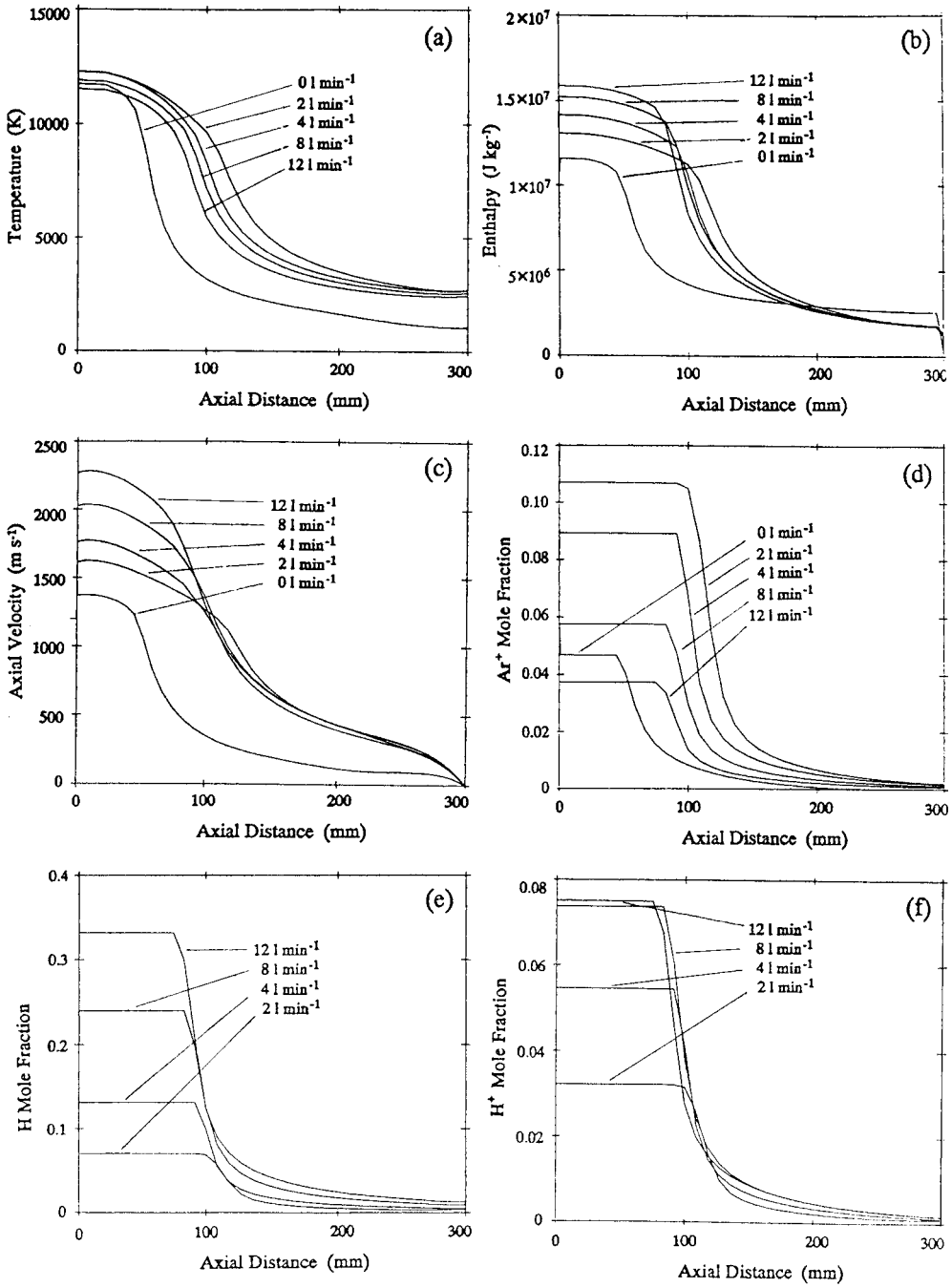

Figure 9. Distributions of: (a) temperature; (b) enthalpy; (c) axial velocity; (d) Ar^+ mole fraction; (e) H mole fraction; and (f) H^+ mole fraction along the plasma jet axis for different H_2 flow rates.

of 50 mm and the plasma jet is relatively short. This is partly because the pure Ar plasma has a lower gas velocity, and partly because the total fraction of dissociated/ionized species is lower

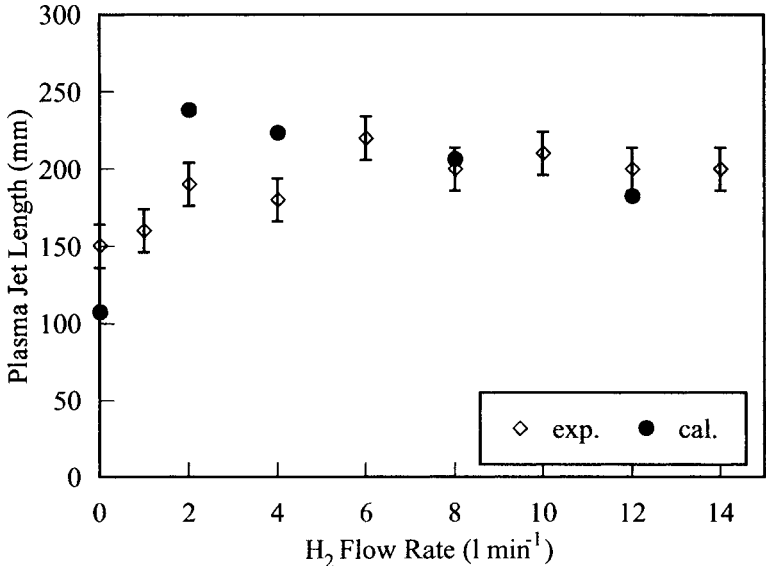

Figure 10. Relationship between plasma jet length and H_2 flow rate.

than that in an Ar + H_2 plasma, and therefore less heat is released from the recombination reactions along the plasma jet. With increasing H_2 flow rate, both the calculated and measured plasma jet length first increases and then decreases slightly, because the plasma gas temperature first increases and then decreases. However, a slight difference exists between the calculations and measurements in the critical H_2 flow rate at which the plasma jet is maximum.

4.2.4. Chamber pressure. Figures 11(a)–(f) show the variation of plasma gas temperature, enthalpy, velocity, and Ar^+, H and H^+ mole fractions as a function of axial distance along the plasma jet axis, respectively, for different chamber pressure of 5, 15, 25 and 35 kPa with constant $I = 700$ A, $F_{Ar} = 35$ l min^{-1} and $F_{H_2} = 8$ l min^{-1}. Increasing chamber pressure strongly reduces the initial and subsequent plasma gas velocity as shown in figure 11(c). Increasing chamber pressure does not change the plasma energy input rate, but increases plasma temperature and H mole fraction while decreasing the plasma enthalpy, and Ar^+ and H^+ mole fractions within an axial distance of 100 mm, as shown in figures 11 (a), (b) and (d)–(f). However, the effect is not significant except at a low chamber pressure of 5 kPa when there is a long plasma jet because of the very high axial jet velocities.

Figure 12 shows the variation of both calculated and measured plasma jet length with chamber pressure. At a chamber pressure of 5 kPa, the plasma gas velocity increases significantly as shown in figure 11(c) and results in a relatively long plasma jet. Unfortunately, the calculated plasma jet length at a chamber pressure of 5 kPa is unlikely to be accurate, because the substrate is placed at a distance of 300 mm from the plasma gun in the calculations as shown in figure 1. Consequently, the measured plasma jet length is 310 mm whereas the calculated plasma jet is ∼400 mm, as shown in figure 12. When the chamber pressure is increased to 15 kPa, the plasma jet length decreases significantly to ∼200 mm for both experiment and calculation. When chamber pressure varies between 15 and 35 kPa, the calculated plasma jet length remains approximately constant whereas there is a slight trend for the measured length to decrease.

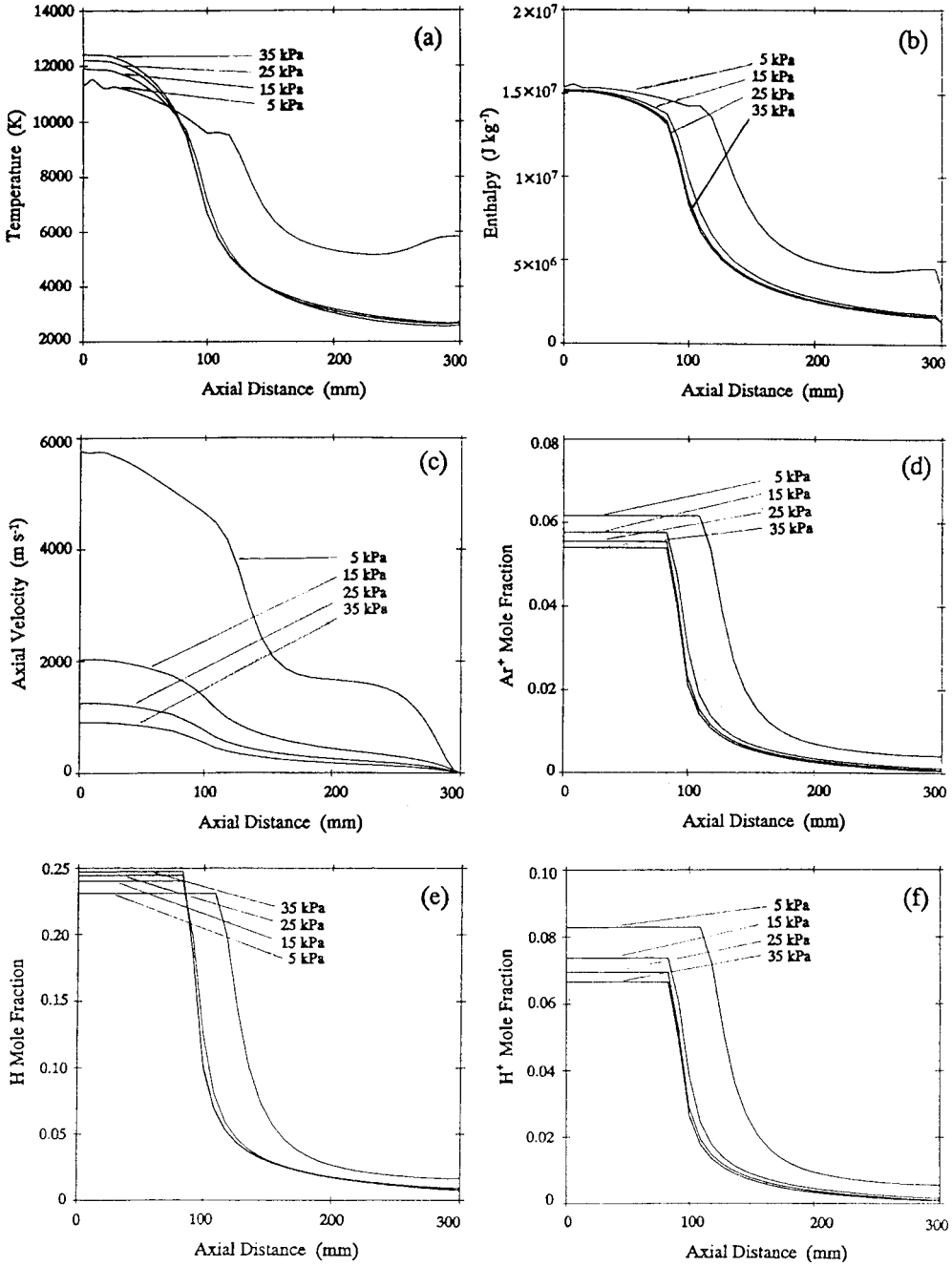

Figure 11. Distributions of: (a) temperature; (b) enthalpy; (c) axial velocity; (d) Ar^+ mole fraction; (e) H mole fraction; and (f) H^+ mole fraction along the plasma jet axis for different chamber pressures.

4.3. Particle temperature and velocity

4.3.1. Particle trajectory. Figure 13 shows the mean trajectories of the 60 Ti particle injections, with an initial temperature of 298 K and initial velocity of zero. Most particles

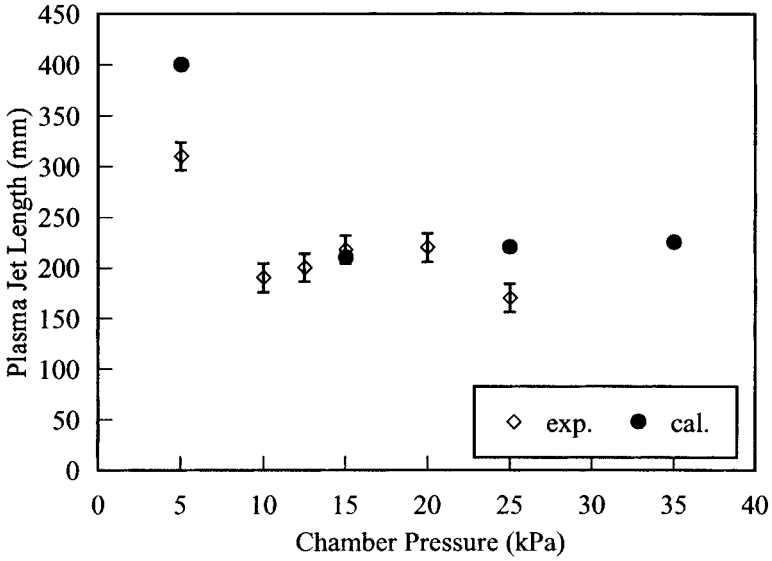

Figure 12. Relationship between plasma jet length and chamber pressure.

move in straight lines, and the larger the initial radial position of the particle then the greater the angle between the particle trajectory and the plasma jet axis, with a maximum angle of 22° for particles at the plasma gun exit edge. The particles with initial positions within a radius of 5.2 mm at the plasma gun exit impact on the substrate, while the particles with initial positions closer to the edge of the orifice miss the substrate and reach the chamber wall. The trajectories of the smallest particles may be more complicated as they become seeded in the larger scale chamber recirculating flow, as shown in figure 13.

4.3.2. Effect of particle size. Figures 14(a) and (b) show the temperatures and axial velocities as a function of axial distance for the 20, 60, 100, 150 and 250 μm Ti particles with an initial temperature of 298 K and an initial velocity of zero at initial radial positions of 0.4, 0.3, 0.2 and 0.1 mm, respectively. For all particles, the temperature and velocity both increase rapidly up to an axial distance of ∼100 mm and then further increase or decrease relatively little until deposition at 300 mm. At a given axial distance, the particle temperature and velocity both decrease sharply with increasing particle size. At the substrate, the temperatures of the 20, 60, 100, 150 and 250 μm particles are 1850, 950, 710, 590 and 485 K, respectively, all below the melting point of Ti of 1933 K [55]. The corresponding particle velocities are 1140, 510, 340, 245 and 160 m s^{-1}, respectively.

4.3.3. Effect of particle injection position. Figures 15(a) and (b) show the temperatures and axial velocities as a function of axial distance for 60 μm Ti particles with an initial temperature of 298 K and an initial velocity of zero at initial radial positions of 0.3, 1.8, 3.3 and 4.8 mm. For all particles, the temperature and velocity histories are almost identical for the first 20–50 mm. Beyond this axial distance, particle temperature and velocity both decrease with increasing initial radial position so that at deposition at 300 mm, the 60 μm Ti particles have a wide range of thermal and velocity conditions. Ideally, to ensure complete particle melting at deposition, the method of powder injection to the gun must be designed carefully to inject particles into the core of the plasma jet.

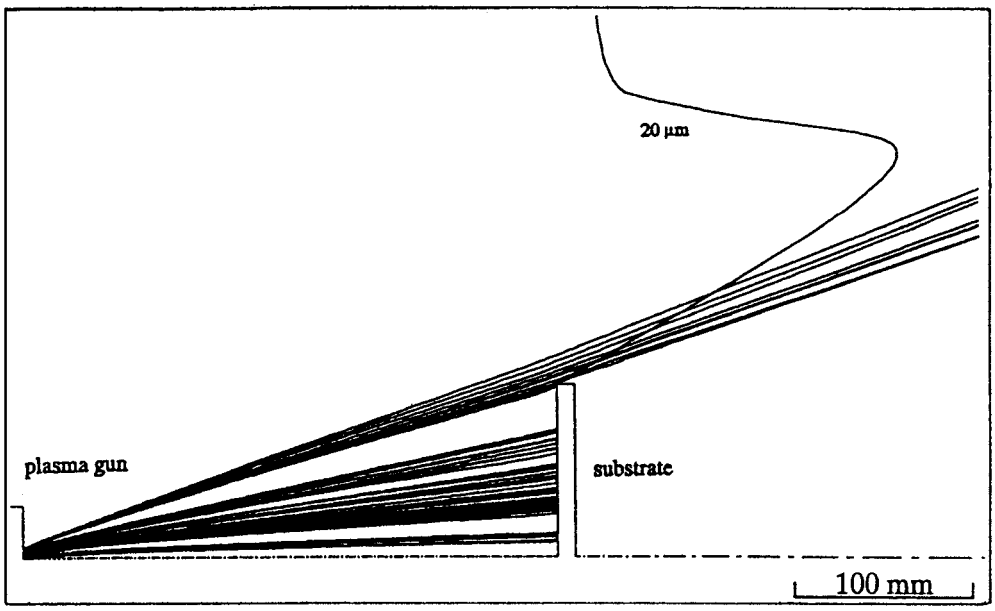

Figure 13. Trajectories of particles.

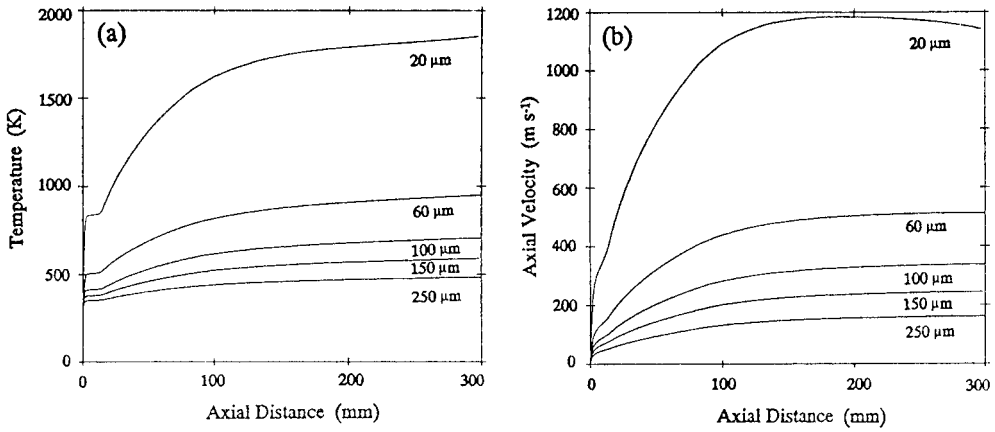

Figure 14. Variations of: (a) particle temperatures; and (b) particle velocities along the plasma jet axis with particle size.

4.3.4. Effect of initial particle temperature and velocity. Figure 16 shows the temperature variations as a function of axial distance for the 20, 60, 100, 150 and 250 μm Ti particles with an initial temperature of 800 K and a velocity of 10 m s^{-1} at initial radial positions of 0.4, 0.3, 0.2 and 0.1 mm, respectively. In comparison with figure 14(a), there is a significant increase in all particle temperatures so that at an axial distance of 300 mm, 20, 60, 100, 150 and 250 μm particles have temperatures of ~2200, 1400, 1200, 1100 and 950 K, respectively. However, the calculated particle temperatures in figures 14(a) and 16 are significantly lower than those expected on the basis of experimental results under identical conditions [2], which showed that particles <100 μm were usually fully or nearly fully molten. Calculation errors result mainly from the following assumptions.

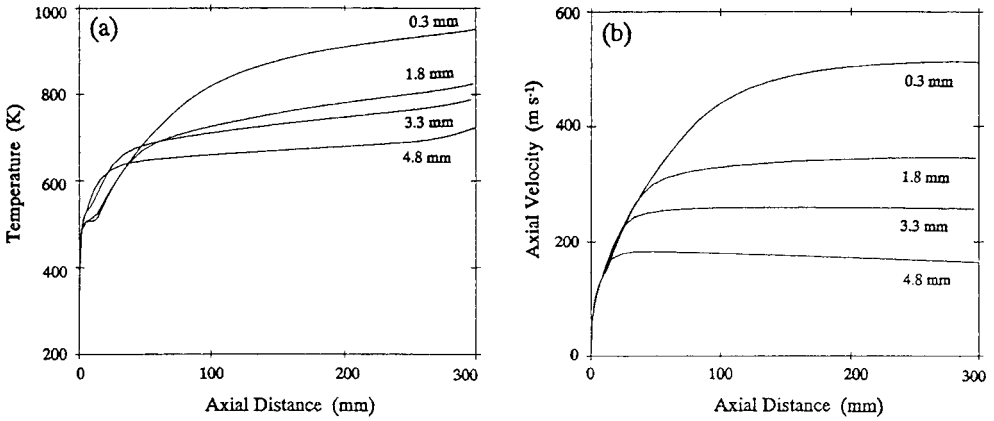

Figure 15. Variations of: (a) particle temperatures; and (b) particle velocities along the plasma jet axis with initial particle position.

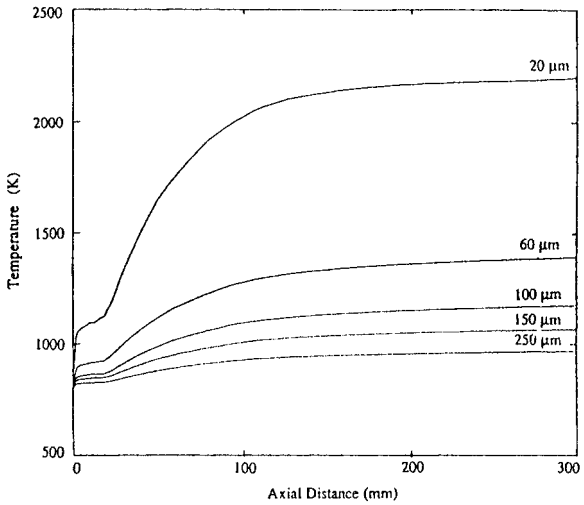

Figure 16. Temperature variations of differently sized particles with an initial temperature of 800 K.

(1) The initial Ti particle temperature is assumed to be either room temperature or 800 K, but in the supporting experiments [2] the particle temperatures could be much higher because the particles were injected into the plasma gun nozzle radially with a slight negative angle of $\sim 5^{\circ}$ and travelled ~ 10 mm in the hottest part of the plasma jet before exiting the plasma gun; and
(2) The Ti particles are assumed to be spherical, but in practice the particles were non-spherical [2], and therefore have greater surface areas than spherical particles of equivalent volume.

5. Conclusions

A numerical model has been developed to calculate the spatial distributions of plasma gas temperature, enthalpy, velocity, and Ar^{+}, H and H^{+} mole fractions, and the particle trajectory,

temperature and velocity in an $Ar + H_2$ plasma jet under a series of VPS processing conditions, using FLUENT V4.2 and incorporating dissociation, ionization and recombination reactions in the plasma gases. The model shows:

(1) Increasing plasma current increases the plasma gas temperature, enthalpy, velocity, and Ar^+ and H^+ mole fractions at all axial distances within 100 mm from the plasma gun.
(2) Increasing H_2 flow rate increases the plasma gas enthalpy, velocity, and H and H^+ mole fractions at all axial distances within 100 mm. The plasma gas temperature and Ar^+ mole fraction have maxima at a H_2 flow rate of 2 l min^{-1}.
(3) Increasing Ar flow rate increases the plasma gas temperature, enthalpy, and Ar^+, H and H^+ mole fractions close to the plasma gun, but they then increase in the region between 50 and 150 mm away from the gun. The plasma gas velocity increases throughout the plasma jet.
(4) Chamber pressure does not have significant effect on the plasma gas temperature, enthalpy, and Ar^+, H and H^+ mole fractions. Increasing chamber pressure, however, decreases the plasma gas velocity significantly.
(5) The plasma jet length increases with increasing plasma current and decreasing Ar flow rate and chamber pressure, and shows a maximum with varying H_2 flow rate. The predictions of the model agree reasonably well with experimental observations of plasma jet length.
(6) Particle temperature and velocity in the plasma jet decrease sharply with increasing particle size and initial radial position at the plasma gun exit. Both particle temperature and velocity increase rapidly in the first 100 mm of the plasma jet, and then become nearly constant for axial distances >150 mm.

Acknowledgments

We would like to thank the UK Engineering and Physical Sciences Research Council, The British Council, The Chinese Education Commission and The Royal Society for financial support.

References

[1] Dearnley P A and Roberts K A 1991 *Powder Metall.* **34** 23
[2] Zhao Y Y, Grant P S and Cantor B 1993 *J. Physique* IV **3** 1685
[3] Grant P S, Zhao Y Y, Li J H, Jenkins M L and Cantor B 1995 *Science and Technology of Rapid Solidification and Processing Technologies* ed M A Otooni (Netherlands: Kluwer) p 109
[4] Zhao Y Y, Grant P S and Cantor B 1995 *Recent Advances in Titanium Metal Matrix Composites* ed F H Froes and J Storer (Pennsylvania: TMS) p 55
[5] Grant P S, Hambleton R, Zhao Y Y, O'Reilly K A Q and Cantor B 1995 *Surface Modification Technologies VIII* ed T S Sudarshan and M Jeadin (London: The Institute of Materials) p 783
[6] Fan Z, Grant P S and Cantor B 1997 *Key Eng. Mater.* **127–131** 335
[7] Baik K-H and Grant P S 1997 *Proc. 5th Eur. Conf. on Advanced Materials, Processes and Applications* vol 1, ed L A J Sarton and H B Zeedijk (Zwijndrecht, Netherlands: Netherlands Society for Material Science) p 341
[8] Baik K-H and Grant P S 1998 *Thermal Spray, Meeting the Challenges of the 21st Century* ed C Coddet (Novelty, OH: ASM) p 1193
[9] Varacalle D J Jr 1991 *Thermal Spray Research and Applications* ed T Bernecki (Novelty, OH: ASM) p 271
[10] Heimann P B, Lamy D and Sopkow T N 1991 *Thermal Spray Research and Applications* ed T Bernecki (Novelty, OH: ASM) p 491
[11] Bisgaard S 1991 *Thermal Spray Research and Applications* ed T Bernecki (Novelty, OH: ASM) p 661
[12] Hermanek F and Riggs W L 1991 *Thermal Spray Research and Applications* ed T Bernecki (Novelty, OH: ASM) p 695
[13] Riggs W L II, Betts R K and Jayaraman N 1991 *Thermal Spray Research and Applications* ed T Bernecki (Novelty, OH: ASM) p 711

[14] Walter J and Riggs W L II 1991 *Thermal Spray Research and Applications* ed T Bernecki (Novelty, OH: ASM) p 729
[15] Chon T *et al* 1992 *Thermal Spray Coatings: Properties, Processes and Applications* (Novelty, OH: ASM) p 3
[16] Steeper T J *et al* 1992 *Thermal Spray Coatings: Properties, Processes and Applications* (Novelty, OH: ASM) p 13
[17] Willen W S 1992 *Thermal Spray Coatings: Properties, Processes and Applications* (Novelty, OH: ASM) p 21
[18] Fauchais P *et al* 1988 *Thermal Spray: Advances in Coatings Technology* ed D L Houck (Metals Park, OH: ASM) p 11
[19] Pfender E 1988 *Surf. Coatings Technol.* **1** 1
[20] Herman H 1988 *Mater. Res. Soc. Bull.* **13** 60
[21] Apelian D *et al* 1983 *Int. Metals Rev.* **28** 271
[22] Fauchais P *et al* 1989 *Metall. Trans.* B **20** 263
[23] Fincke J R *et al* 1994 *Int. J. Heat Mass Transfer* **37** 1673
[24] Vardelle M *et al* 1983 *J. Am. Inst. Chem. Eng.* **29** 236
[25] Wei D, Apelian D and Farouk 1985 *Proc. 7th Int. Symp. on Plasma Chem.* ed C J Timmermans (New York: Pergamon) p 810
[26] Takeda K, Hayashi K and Ohashi T 1985 *Proc. 7th Int. Symp. on Plasma Chem.* ed C J Timmermans (New York: Pergamon) p 848
[27] Dilawari A H and Szekely J 1987 *Plasma Processing and Synthesis of Materials* ed D Apelian and J Szekely (Pittsburgh, PA: Materials Research Society) p 3
[28] Wei D Y C, Apelian D and Farouk B 1987 *Plasma Processing and Synthesis of Materials* ed D Apelian and J Szekely (Pittsburgh, PA: Materials Research Society) p 77
[29] Fincke J R, Jeffery C L and Englert S B 1987 *Plasma Processing and Synthesis of Materials* ed D Apelian and J Szekely (Pittsburgh, PA: Materials Research Society) p 127
[30] Harris D and Kelly M 1987 *Plasma Processing and Synthesis of Materials* ed D Apelian and J Szekely (Pittsburgh, PA: Materials Research Society) p 141
[31] Self S A 1987 *Plasma Processing and Synthesis of Materials* ed D Apelian and J Szekely (Pittsburgh, PA: Materials Research Society) p 183
[32] Varacalle D J, Reynolds L D and Shaw C B Jr 1987 *Plasma Processing and Synthesis of Materials* ed D Apelian and J Szekely (Pittsburgh, PA: Materials Research Society) p 49
[33] Wei D Y C, Farouk B and Apelian D 1987 *Plasma Processing and Synthesis of Materials* ed D Apelian and J Szekely (Pittsburgh, PA: Materials Research Society) p 41
[34] Chyou T W and Pfender E 1987 *Proc. 8th Int. Symp. on Plasma Chem.* vol 1, ed K Akashi and A Kinbara (Research Triangle Park, NC: International Union of Pure & Applied Chemists) p 101
[35] Fleck E, Lee Y C and Pfender E 1987 *Proc. 8th Int. Symp. on Plasma Chem.* vol 1, ed K Akashi and A Kinbara (Research Triangle Park, NC: International Union of Pure & Applied Chemists) p 392
[36] Vardelle M *et al* 1987 *Proc. 8th Int. Symp. on Plasma Chem.* vol 1, ed K Akashi and A Kinbara (Research Triangle Park, NC: International Union of Pure & Applied Chemists) p 404
[37] Wei D Y, Apelian D and Farouk B 1989 *Metall. Trans.* B **20** 251
[38] Pfender E, Chen W L T and Spores R 1991 *Thermal Spray Research and Applications* ed T Bernecki (Novelty, OH: ASM) p 1
[39] Fincke J R and Swank W D 1991 *Thermal Spray Research and Applications* ed T Bernecki (Novelty, OH: ASM) p 39
[40] Roman W C *et al* 1991 *Thermal Spray Research and Applications* ed T Bernecki (Novelty, OH: ASM) p 49
[41] Hedges M A and Taylor R 1991 *Thermal Spray Research and Applications* ed T Bernecki (Novelty, OH: ASM) p 59
[42] Vardelle M *et al* 1991 *Thermal Spray Research and Applications* ed T Bernecki (Novelty, OH: ASM) p 65
[43] Fincke J R and Swank W D 1992 *Thermal Spray Coatings: Properties, Processes and Applications* (Novelty, OH: ASM) p 193
[44] Fauchais P *et al* 1992 *Thermal Spray Coatings: Properties, Processes and Applications* (Novelty, OH: ASM) p 205
[45] Vardelle D J and Riggs W L II 1992 *Thermal Spray Coatings: Properties, Processes and Applications* (Novelty, OH: ASM) p 245
[46] Vardelle M, Vardelle A and Grimaud A 1991 *Proc. 2nd Plasma-Technik-Symposium* vol 1 (Wohlen, Switzerland: Plasma-Technik AG)p 151
[47] Chang C H 1992 *Thermal Spray: International Advances in Coatings Technology* (Metals Park, OH: ASM) p 793
[48] Njah Z *et al* 1993 *Int. J. Heat Mass Transfer* **36** 3897

[49] Pfender E 1994 *Thin Solid Films* **238** 228
[50] Rahmane M, Soucy G and Boulos M I 1994 *Int. J. Heat Mass Transfer* **37** 2035
[51] Planche M P *et al* 1994 *Thermal Spray Industrial Applications* ed C C Berndt and S Sampath (Novelty, OH: ASM) p 349
[52] Chang C H and Pfender E 1996 *JOM* **48** 46
[53] Zhao Y Y, Grant P S and Cantor B 2000 *Modelling Simul. Mater. Sci. Eng.* **8** 497
[54] Starling S G and Woodall A J 1950 *Physics* (London: Longmans Green) p 761
[55] Lide D R 1996 *CRC Handbook of Chemistry and Physics* 77th edn (Boca Raton, FL: CRC Press) section 6, p 19
[56] Plapp J E 1968 *Engineering Fluid Mechanics* (Englewood Cliffs, NJ: Prentice-Hall) p 72
[57] White F M 1994 *Fluid Mechanics* 3rd edn (New York: McGraw-Hill)
[58] FLUENT Inc 1993 *FLUENT V4.2 Manual* (Lebanon, NH: FLUENT)
[59] Ward-Smith A J 1980 *Internal Fluid Flow—The Fluid Dynamics of Flow in Pipes and Ducts* (Oxford: Clarendon) p 46
[60] Howatson A M 1965 *An Introduction to Gas Discharges* (Oxford: Pergamon) pp 114–17
[61] Kubin R F and Presley L L 1964 *Thermodynamic Properties and Mollier Chart for Hydrogen from 300 K to 20 000 K* (Washington DC: NASA) pp 4–20
[62] Matejka D and Benko B 1989 *Plasma Spraying of Metallic and Ceramic Materials* (New York: Wiley) p 26
[63] Underhill R P, Grant P S, Cantor B and Bryant D J 1997 *Int. J. Non-Equilib. Proc.* **10** 201
[64] Zhao Y Y 1995 *DPhil Thesis* Oxford University